

1 **Narrow, fast, and “cold” mantle plumes caused by**  
2 **strain-weakening rheology in Earth’s lower mantle**

3 **Anna J. P. Gülcher<sup>1</sup>, G. J. Golabek<sup>2</sup>, M. Thielmann<sup>2</sup>, M. D. Ballmer<sup>3</sup>, and P.**  
4 **J. Tackley<sup>1</sup>**

5 <sup>1</sup>Institute of Geophysics, Department of Earth Sciences, ETH Zurich, Zurich, Switzerland

6 <sup>2</sup>Bayerisches Geoinstitut, University Bayreuth, Bayreuth, Germany

7 <sup>3</sup>UCL Earth Sciences, University College London, London, UK

8 **Key Points:**

- 9
- 10 • A new strain-weakening (SW) rheology for lower mantle materials is implemented  
11 in numerical models of global-scale mantle convection
  - 12 • Such rheology causes weakening of plume conduits, forming narrow lubrication chan-  
13 nels in the mantle through which hot material easily rises
  - 14 • SW rheology in the lower mantle could explain the discrepancy between expected  
and observed thermal anomalies of deep mantle plumes on Earth

---

Corresponding author: Anna Gülcher, [anna.guelcher@erdw.ethz.ch](mailto:anna.guelcher@erdw.ethz.ch)

15 **Abstract**

16 The rheological properties of Earth’s lower mantle are key for mantle dynamics and  
 17 planetary evolution. The main rock-forming minerals in the lower mantle are bridgman-  
 18 ite (Br) and smaller amounts of ferropericlase (Fp). Previous work has suggested that  
 19 the large differences in viscosity between these minerals greatly affect the bulk rock rhe-  
 20 ology. The resulting effective rheology becomes highly strain-dependent as weaker Fp  
 21 minerals become elongated and eventually interconnected. This implies that strain lo-  
 22 calization may occur in Earth’s lower mantle. So far, there have been no studies on global-  
 23 scale mantle convection in the presence of such strain-weakening (SW) rheology. Here,  
 24 we present 2D numerical models of thermo-chemical convection in spherical annulus ge-  
 25 ometry including a new strain-dependent rheology formulation for lower mantle mate-  
 26 rials, combining rheological weakening and healing terms. We find that SW rheology has  
 27 several direct and indirect effects on mantle convection. The most notable direct effect  
 28 is the changing dynamics of weakened plume channels as well as the formation of larger  
 29 thermochemical piles at the base of the mantle. The weakened plume conduits act as lu-  
 30 brication channels in the mantle and exhibit a lower thermal anomaly. SW rheology also  
 31 reduces the overall viscosity, notable in terms of increasing convective vigor and core-  
 32 mantle boundary (CMB) heat flux. Finally, we put our results into context with exist-  
 33 ing hypotheses on the style of mantle convection and mixing. Most importantly, we sug-  
 34 gest that the new kind of plume dynamics may explain the discrepancy between expected  
 35 and observed thermal anomalies of deep-seated mantle plumes on Earth.

36 **Plain Language Summary**

37 Earth’s lower mantle (660-2890 km depth) controls our planet’s evolution by reg-  
 38 ulating the transport of materials and heat through mantle convection. To better un-  
 39 derstand mantle convection and the evolution of Earth over billions of years, mathemat-  
 40 ical laws describing how rocks flow (viscosity) are needed. Recently, it was discovered  
 41 that the deformation history of lower-mantle rocks affects the viscosity. In the lower man-  
 42 tle there are two main minerals: Bridgmanite (Br), which is relatively strong (high vis-  
 43 cosity), and ferropericlase (Fp), which is relatively weak (low viscosity). When a rock  
 44 containing both minerals is deformed, the weak Fp grains can form interconnected lay-  
 45 ers, lowering the overall viscosity and thus weakening the whole rock.

46 Here, we present prompting new results that show how mantle convection and Earth’s  
 47 evolution are affected by such a deformation-dependent or “strain-weakening” (SW) vis-  
 48 cosity law, using global-scale numerical simulations of mantle convection and plate tec-  
 49 tonics. We find that, in particular, the dynamics of hot, rising columns of mantle ma-  
 50 terial (plumes) are affected by SW rheology, making them more narrow, fast, and less  
 51 hot relatively to other plumes. Finally, we find that this new types of plume dynamics  
 52 could be linked to several observations of mantle plumes in the Earth.

53 **1 Introduction**

54 Solid-state convection of the rocky, 2980-km deep mantle shapes the evolution of  
 55 Earth’s interior and surface over billions of years. The style of mantle convection and  
 56 its temporal evolution is therefore subject to active research. At least in the lower man-  
 57 tle, Earth’s convective system is dominated by a degree-2 pattern, with two broad, an-  
 58 tipodal, equatorial regions of upwellings surrounded by sheets of downwellings. The con-  
 59 vective system is further characterised by existence of several geochemically distinct (and  
 60 perhaps long-term isolated) reservoirs within (e.g., Garnero & McNamara, 2008; Dziewon-  
 61 ski et al., 2010; Torsvik et al., 2010). The two large low shear-wave velocity (LLSVP)  
 62 piles in Earth’s lowermost mantle spatially correlate with the two antipodal upwelling  
 63 regions, and their edges seem to match with hotspot locations at the surface (Torsvik

64 et al., 2010; M. Li & Zhong, 2017). Since plumes can serve as an absolute reference frame  
 65 for plate reconstructions (e.g., Wilson, 1963), their temporal stability at their root and  
 66 any deflections during upwelling are important to establish. Even though mantle plumes  
 67 are an intrinsic part of Earth’s convection system, their dynamics, geometries, and fix-  
 68 ity remain poorly understood since they were first proposed (Morgan, 1971).

69 To date, it is understood that mantle plumes can start as deep as the core–mantle  
 70 boundary and rise all the way to the base of the lithosphere, where they sustain intraplate  
 71 hotspot volcanism (Morgan, 1971). In the classical view (Howard, 1964; Richards et al.,  
 72 1989), a rising mantle plume is characterized by a large head atop a narrow tail, although  
 73 chemical complexities may result in deviations from such classical shapes (Farnetani &  
 74 Samuel, 2005; Davaille & Vatteville, 2005; Lin & Van Keken, 2006). Plume shapes are  
 75 difficult to clearly be imaged by seismic tomography due to wavefront healing (Ritsema  
 76 et al., 2021). Although recent full-waveform tomography models hint at the presence of  
 77 plume-like features associated with major hotspots (e.g. French & Romanowicz, 2015),  
 78 ambiguity remains as to the vertical continuity of these features, as well as their shapes  
 79 and stability (e.g., Wolfe et al., 2009; French & Romanowicz, 2015; Davaille & Romanow-  
 80 icz, 2020). Another controversy lies in the temperature excess of such mantle plumes.  
 81 Excess temperatures are estimated to be 100-300 K, which is significantly lower than the  
 82 expected CMB temperature difference of  $\sim 1000$  K (Boehler, 1996). While the dynam-  
 83 ics and shapes of plumes are well studied in geodynamic models with Newtonian rhe-  
 84 ology, they strongly depend on the material properties of mantle rocks (e.g. Massmeyer  
 85 et al., 2013). However, these properties, and in particular the rheology of the lower man-  
 86 tle, are ill-constrained.

87 The two main constituents of the lower mantle are bridgmanite (Br) and ferroper-  
 88 iclase (Fp) (Hirose, Morard, et al., 2017). The viscosity of the strong mineral bridgman-  
 89 ite ( $\eta_{\text{Br}} = 10^{21} - 10^{23}$  Pa·s) is several orders of magnitude larger than that of the weak  
 90 ferropericlase ( $\eta_{\text{Fp}} = 10^{18} - 10^{21}$  Pa·s) (Yamazaki & Karato, 2001; Kaercher et al., 2016).  
 91 It has been suggested that for typical mantle rocks that comprise Br as well as Fp, the  
 92 bulk viscosity of the rock decreases with ongoing deformation as the weaker ferroperi-  
 93 clase crystals become elongated in the direction of strain and interconnect with each other  
 94 (Girard et al., 2016) (see Fig. 1a). This experimental result was further confirmed in nu-  
 95 merical studies on the effective rheology of a lower-mantle two-phase medium during de-  
 96 formation (e.g., Thielmann et al., 2020; de Montserrat et al., 2021). The weakening of  
 97 the bulk rock with accumulating strain (“strain weakening”) implies that deformation  
 98 may localize in the lower mantle, analogous to localized shear zones in crustal rocks. Such  
 99 strain localization may potentially explain the isolation of large unmixed domains in the  
 100 lower mantle, which may host primordial (or “hidden”) geochemical reservoirs away from  
 101 regions of localized deformation (Chen, 2016; Ballmer et al., 2017; Mundl et al., 2017;  
 102 Gülcher et al., 2020) (see Fig. 1b). However, the effects of strain weakening on lower-  
 103 mantle convection patterns and mixing dynamics have not yet been studied using global-  
 104 scale geodynamic models.

105 Here, we implement a macro-scale description of strain-weakening (SW) rheology  
 106 in a global mantle convection model. We present 2D numerical models of thermochem-  
 107 ical convection in a spherical annulus geometry that include a new implementation of  
 108 tracking the strain ellipse at each tracer through time. We allow lower mantle materi-  
 109 als to rheologically weaken to various degrees and investigate the effects of this rheolog-  
 110 ical weakening on mantle convection dynamics. We particularly focus on the character-  
 111 istics of mantle plumes in the models. We find that SW rheology has several effects on  
 112 mantle dynamics, including on the (i) pattern of mantle flow, (ii) thermal evolution of  
 113 the mantle, (iii) pile stability, and (iv) mantle plume dynamics. We distinguish first-order  
 114 effects (directly caused by spatial viscosity variations resulting from SW rheology) and  
 115 second-order effects (indirectly caused by a changing Rayleigh number caused by SW  
 116 of ambient mantle), and link the results to the previously-proposed style of mantle con-

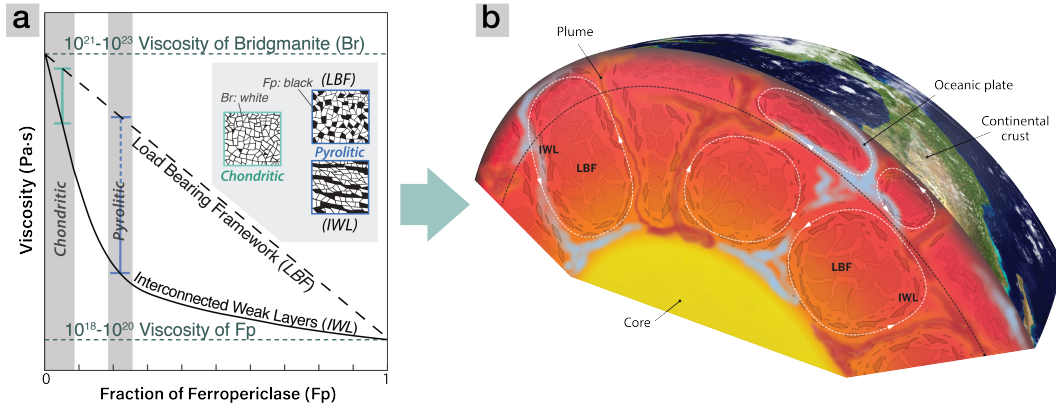


**Figure 1.** (a) Variation of the bulk viscosity of Br-Fp mixtures as a function of Fp fraction for the two end-member textures of “load-bearing framework” (LBF) and non-linear “interconnected weak layers” (IWL) (Handy, 1994). Image adapted from Ballmer et al. (2017). (b) Suggested mantle convection dynamics in which shear localization of weak Fp grains induces weak layers of “interconnected frameworks” (IWL) along slabs and plumes, and mixing is less efficient for the bridgmanitic “load-bearing framework” (LBF) part of the lower mantle, potentially promoting the preservation of long-lived geochemical reservoirs. From (Chen, 2016). Reprinted from Chen (2016), Copyright (2016), with permission from The American Association for the Advancement of Science (AAAS).

117 vection (Fig. 1b). The changing plume dynamics are of particular interest since weak-  
 118 ened plumes could explain the discrepancy between expected and observed thermal anom-  
 119 alies of deep-seated mantle plumes on Earth.

## 120 2 Methods

### 121 2.1 Numerical technique and model set-up

122 In this study, we use the finite-volume code StagYY (Tackley, 2008) to model man-  
 123 tle convection in two-dimensional spherical annulus geometry (Hernlund & Tackley, 2008).  
 124 The conservation equations for mass, momentum, energy and composition are solved on  
 125 a staggered grid for a compressible fluid with an infinite Prandtl number. The compu-  
 126 tational domain is discretized by  $1024 \times 128$  cells, in which  $\sim 2.5$  million tracers, track-  
 127 ing composition, temperature, and strain, are advected (20 tracers per cell). Due to ver-  
 128 tical grid refinement near the boundary layers and near 660 km depth, the size of grid  
 129 cells varies between 4 and 25 km in the vertical direction. Free-slip and isothermal bound-  
 130 ary conditions are employed at the top and bottom boundaries, with a fixed surface tem-  
 131 perature of 300 K and CMB temperature of 4000 K. The numerical experiments are purely  
 132 bottom heated (i.e., no internal heating).

133 Initial mantle temperatures are calculated from an adiabat with a potential tem-  
 134 perature of 1900 K, together with the top and bottom boundary layers, and superim-  
 135 posing small random temperature perturbations of  $\pm 10$  K on the cell level. The result-  
 136 ing temperature profile is  $\sim 300$  K warmer than Earth’s present-day geotherm. Such high  
 137 initial mantle temperatures are applied to crudely mimic the thermal evolution of the  
 138 mantle, with higher convective vigor and widespread near-surface melting in the early  
 139 model evolution (e.g., Davies, 2007; Herzberg et al., 2010).

Depth [km]	Temperature [K]	$\Delta\rho_{pc}$ [kg/m <sup>3</sup> ]	Phase change width [km]	$\gamma$ [MPa/K]	$K_0$ [GPa]; $K'_0$ [GPa/GPa]	depth range [km]
<i>Olivine</i> ( $\rho_{surf} = 3240 \text{ kg/m}^3$ )						
410	1600	180	25	+2.5	163; 3.9	0-410
660	1900	435	25	-2.5	85; 3.9	410-660
2740	2300	61.6	25	+10	210; 4.0	660-2740
<i>Pyroxene-garnet</i> ( $\rho_{surf} = 3080 \text{ kg/m}^3$ )						
40	1000	350	25	0	163; 3.9	0-40
300	1600	100	75	+1.0	130; 3.9	40-300
720	1900	350	75	+1.0	85; 3.9	300-720
2740	2300	61.6	25	+10	210; 4.0	720-2740
						2740-2890

**Table 1.** Phase change parameters used in this study for the olivine and pyroxene-garnet systems. The table shows the depth and temperature at which a phase transition occurs;  $\Delta\rho_{pc}$  and  $\gamma$  denote the density jump across the phase transition and the Clapeyron slope, respectively. The Clapeyron slopes for these phase changes are similar to those used in previous numerical studies (e.g., Tackley et al., 2013). In the olivine system, the 410 and 660 phase changes are made discontinuous, whereas all other phase changes in all systems are defined as hyperbolic tangent functions (*tanh*) that transition between the phases across a predefined phase loop width. Finally,  $K_0$  refers to the reference bulk modulus for the system for each individual layer (marked by the depth range), and  $K'_0$  refers to its pressure-derivative.

140

## 2.2 Treatment of mantle composition, phase changes and melting

141

142

143

144

145

146

147

148

149

150

151

152

153

154

The driving forces of mantle convection are related to rock density, which depends on temperature and composition (Nakagawa & Buffett, 2005; Tackley et al., 2013). Composition in our modelled mantle has two lithological components: harzburgite and basalt. Accordingly, each tracer carries a mechanical mixture of harzburgite and basalt. Initially, all tracers in the model carry a mechanical mixture of 80% harzburgite and 20% basalt (i.e., pyrolitic composition). Both end-member materials are treated as a mixture of olivine and pyroxene-garnet systems that undergo different solid-solid phase transitions (for details, see Nakagawa et al., 2010). Harzburgite is considered to be a mixture of 75% olivine and 25% pyroxene-garnet; basalt is considered as pure pyroxene-garnet. The resulting density profiles of harzburgite and MORB are consistent with those from (Xu et al., 2008). Compositional anomalies carried on tracers evolve from the initial state due to melt-induced differentiation: they undergo partial melting as a function of pressure, temperature and composition to sustain the formation of basaltic crust, and leaving a harzburgitic residue (for details, see Nakagawa et al., 2010).

155

## 2.3 Visco-plastic rheology

156

157

158

Deformation in the mantle is resisted by viscous stresses. Viscosity is temperature-, pressure-, composition- (or phase-), and strain-dependent following an Arrhenius-type viscosity law (Newtonian rheology):

$$\eta(T, P, c) = \eta_0 \cdot \lambda_c \cdot f_w \cdot \exp\left(\frac{E_a + P \cdot V_a}{R \cdot T} - \frac{E_a}{R \cdot T_0}\right) \quad (1)$$

159

160

161

162

where  $\eta_0$  is the reference viscosity at zero pressure and reference temperature  $T_0$  (= 1600 K),  $E_a$  and  $V_a$  are the activation energy and volume, respectively,  $T$  is the absolute temperature,  $P$  the pressure, and  $R$  is the gas constant (8.314 J·mol<sup>-1</sup> K<sup>-1</sup>). Composition-dependency is considered through prefactor  $\lambda_c$ : a viscosity increase of one order of mag-

Property	Symbol	Value	Units
Mantle domain thickness	$D$	2890	km
Gravitational acceleration	$g$	9.81	m/s <sup>2</sup>
Surface temperature	$T_s$	300	K
CMB temperature	$T_{\text{CMB}}$	4000	K
Reference viscosity	$\eta_0$	$5 \cdot 10^{20}$	Pa·s
PV viscosity contrast	$\lambda_{\text{pv}}$	10	
PPV viscosity contrast	$\lambda_{\text{ppv}}$	$10^{-3}$	
Reference temperature	$T_0$	1600	K
Initial potential temperature	$T_{0,\text{ini}}$	1900	K
Activation energy	$E_a$	200	kJ/mol
Activation energy - PPV	$E_{a,\text{PPV}}$	100	kJ/mol
Activation volume	$V_a$	$2.6 \cdot 10^{-6}$	m <sup>3</sup> /mol
Activation volume - PPV	$V_{a,\text{PPV}}$	$1.0 \cdot 10^{-6}$	m <sup>3</sup> /mol
Surface yield stress	$\tau_{\text{yield}}$	30	MPa
Yield stress depth derivative	$\tau'_{\text{yield}}$	0.01	MPa/MPa
Surface specific heat capacity	$C_{\text{P},0}$	1200	J/(kg·K)
Surface thermal conductivity	$k_0$	3	W/(m·K)
Surface thermal expansivity	$\alpha_0$	$3 \cdot 10^{-5}$	K <sup>-1</sup>

**Table 2.** Physical properties used in the simulations of this study. PV = perovskite; PPV = post-perovskite. Since we solve for compressible convection, the adiabatic temperature, density, thermal conductivity, thermal expansivity, and heat capacity are pressure-dependent following a third-order Birch-Murnaghan equation of state (Tackley et al., 2013).

163 nitude is imposed along the 660-km depth boundary (consistent with e.g., Čížková et al.,  
164 2012), and a viscosity decrease of  $10^{-3}$  relative to the lower mantle is imposed at post-  
165 perovskite phase transition in the lowermost mantle (as suggested by Ammann et al.,  
166 2010). By considering a linear relationship between stress and strain (Newtonian rhe-  
167 ology), the implicit dominant deformation mechanism is diffusion creep. Note however  
168 that we consider an activation energy that is smaller than experimental constraints for  
169 the upper mantle, an approach that can account for the effects of dislocation creep (e.g.,  
170 Christensen & Hofmann, 1994; van Hunen et al., 2005). With our chosen activation en-  
171 ergy and volume, the activation enthalpy in the lower mantle varies from 262 kJ/mol to  
172 548 kJ/mol, in line with perovskite predictions by Yamazaki and Karato (2001). An ad-  
173 ditional strain-dependency of viscosity is implemented through the weakening factor  $f_w$   
174 (see next section). All physical and rheological parameters used in this study are listed  
175 in Table 2.

176 In order to obtain plate-like behavior at the surface, we assume that the material  
177 deforms plastically when a critical pressure-dependent yield stress is reached (as in Tack-  
178 ley, 2000a; Crameri & Tackley, 2014) (see Table 2). Plate-like behavior is evaluated us-  
179 ing diagnostic criteria from (Tackley, 2000b): plateness  $p$  (the degree to which surface  
180 deformation is localized) and mobility  $m$  (the extent to which the lithosphere is able to  
181 move). An ideal plate tectonic style gives  $p = 1$  and  $m$  close to or larger than 1.

## 182 2.4 Strain-dependent rheology

### 183 2.4.1 Finite strain

184 Following the finite deformation approach of (McKenzie, 1979), and building up  
185 on previous work (Xie & Tackley, 2004), the deformation tensor  $M$  is tracked on the trac-

186 ers, which are advected with the flow. At each time step, the velocity gradient tensor  
 187 is calculated and interpolated to the position of each tracer, from which the additional  
 188 deformation for that time step can be retrieved. This additional deformation is then added  
 189 to the existing deformation tensor. A second-order approach is implemented following  
 190 (McKenzie, 1979). This approach tracks stretching, rotation and advection in full ten-  
 191 sor form (Fig. 2a). The eigenvectors of the matrix  $MM^T$  give the principal directions  
 192 of the strain ellipse, and the square root of the eigenvalues of this matrix give the amount  
 193 of strain in each direction (i.e., the semi-major and semi-minor axes  $a$  and  $b$ ). The scalar  
 194 (finite) strain  $\epsilon$  is calculated from the semi-major and semi-minor axes of the strain el-  
 195 lipse (see Supporting Information Text S1 for more detail) and is defined as:

$$\epsilon = \log_{10} \left( \frac{a}{b} \right) \quad (2)$$

196 The deformation matrix  $M$  is reset to a unit matrix when a tracer passes the depth of  
 197 660 km (i.e., the strain ellipse is reset to a circle), representing the resetting of the micro-  
 198 structure of the rock when it passes through a major solid-solid phase transition (e.g.,  
 199 Solomatov & Reese, 2008).

#### 200 **2.4.2 Strain weakening parametrization**

201 Lower-mantle material is rheologically weakened following a simplified strain-dependent  
 202 weakening curve (Fig. 2b):

$$f_w(\epsilon) = 0.5 \cdot (1 + f_w^{\max}) + 0.5 \cdot (f_w^{\max} - 1) * \tanh [C \cdot (\epsilon_i - \epsilon_{\text{crit}})] \quad (3)$$

203 where  $\epsilon_{\text{crit}}$  is the critical strain threshold parameter (the strain at which half of the weak-  
 204 ening has taken place, see Fig. 2b),  $f_w^{\max}$  is the maximum weakening factor (1 for no weak-  
 205 ening), and  $C$  controls shape of strain weakening curve. How this weakening curve trans-  
 206 lates with different strain definitions is discussed in Supporting Information Text S2. As  
 207 proposed by Thielmann et al. (2020) and de Montserrat et al. (2021), weakening occurs  
 208 almost instantaneously as material becomes deformed (see Fig. 2b). The maximum amount  
 209 of weakening ( $f_w^{\max}$ ) is varied between the models. For simplicity, we neglect the composition-  
 210 dependency of strain weakening, as well as the anisotropy of viscosity according to the  
 211 strain tensor, to establish the first-order effects of strain-weakening rheology on the lower  
 212 mantle. Neglecting anisotropy assumes that the strain ellipse is well-aligned with the dom-  
 213 inant shear direction at any finite strain.

#### 214 **2.4.3 Rheological healing**

215 Processes such as diffusion-dominated annealing and/or grain growth may lead to  
 216 the relaxation of deformed grains (e.g. Solomatov & Reese, 2008). For part of the mod-  
 217 els, we approximate such rheological healing by relaxing the deformation matrix (i.e.,  
 218 strain ellipse) towards a unity matrix (i.e., circle) with a temperature-dependent (grain  
 219 growth highly depends on temperature) and pressure-dependent (diffusion is limited at  
 220 higher pressures) term that may represent diffusion creep-dominated healing of micro-  
 221 structures. This lowers the local strain value  $\epsilon$  and subsequently reduces the effective weak-  
 222 ening that occurs. The temperature-dependency of rheological healing allows for long-  
 223 term memory of deformation at cold temperatures and faster healing at deep mantle tem-  
 224 peratures, whereas the pressure-dependency may counteract fast rheological healing at  
 225 high  $T$ - $P$  regions. Rheological healing is implemented as:

$$\frac{dM}{dt} = -H \cdot (M - I) \quad (4)$$

226 where  $H$  is the rheological healing rate ( $H = \frac{1}{\tau_h}$  with reference timescale of rheological  
 227 healing  $\tau_h$ ). Accordingly, the deformation matrix  $M$  is updated as follows:

$$M_{\text{new}} = M_{\text{old}} \cdot \exp(-H \cdot dt) + I \cdot [1 - \exp(-H \cdot dt)] \quad (5)$$

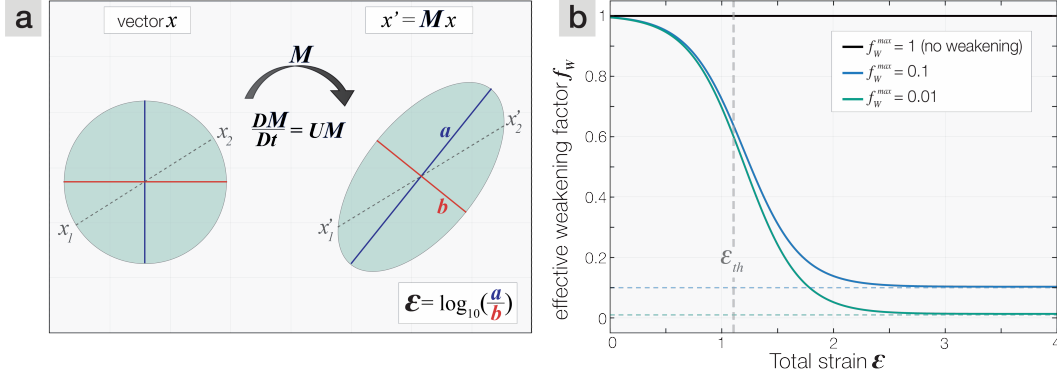


**Figure 2.** (a) The deformation matrix  $M$  relates a vector  $x$  connecting two nearby points at time  $t$  to the same vector at time zero. The time evolution of  $M$  on each tracer can be described by multiplying the velocity gradient tensor  $U$  with  $M$  (for details, see McKenzie, 1979), and  $M$  is updated at each time step on each tracer. (b) Weakening curve applied to all lower mantle materials in the models that explore the effect of strain-dependent rheology in the lower mantle on mantle dynamics (see Section 2.4.3, eq. 3). Input variables are  $f_w^{\max}$  (the maximum weakening factor  $f_w$ ), the critical strain threshold  $\epsilon_{th}$  (the strain at which half of the maximum weakening has taken place after which weakening occurs), and the shape factor  $C$ .

228 Where  $M_{\text{new}}$  is the updated deformation matrix,  $M_{\text{old}}$  is the deformation matrix before  
 229 healing,  $dt$  is the time step in seconds and  $I$  is the unit matrix. The rheological healing  
 230 rate is temperature- and pressure-dependent following:

$$H(T, P) = H_{660} \cdot \exp\left\{ - \left[ \frac{E_a + (P - P_{660}) \cdot V_a}{R \cdot T} - \frac{E_a}{R \cdot T_{660}} \right] \right\} \quad (6)$$

231 where  $H_{660}$  is the reference healing rate ( $\text{s}^{-1}$ ) at the top of the lower mantle (at  $P =$   
 232  $P_{660}$  and  $T = T_{660}$ , along the reference adiabat); this depth is chosen because weak-  
 233 ening and healing only occur in the lower mantle. The activation energy and volume are  
 234 assumed to be the same as those for diffusion creep because atomic (vacancy-) diffusion  
 235 is also the mechanism by which healing occurs. More information on this rheological heal-  
 236 ing rate, the chosen reference values, and how this parametrization ultimately affects the  
 237 distribution of strain in the models is described in Supporting Information Text S2.

## 238 2.5 Automated detection of mantle domains

239 We use the geodynamic diagnostics toolbox StagLab (Cramer, 2018) to automat-  
 240 ically detect regional flows that are either self-driven (i.e., active) or induced (i.e., pas-  
 241 sive). Active regional flows represent mantle plumes (active upwellings) or active slabs  
 242 (active downwellings). We use a new combined thermo-dynamical approach of identi-  
 243 fying mantle plumes and slabs, which is explained in detail in Supporting Information  
 244 Text S3. As a summary, active plumes and slabs are defined based on their anomalies  
 245 in both temperature and radial velocity combined. Finally, the mantle diagnostics rou-  
 246 tine also detects thermochemical piles present atop the CMB (see Text S3). Using this  
 247 routine, the physical properties within all different mantle domains can be separately ex-  
 248 plored.

249

## 2.6 Parameter study

250

251

252

253

254

255

256

257

258

259

260

In this numerical study, we vary several parameters. Most of them are related to the newly-implemented strain-weakening parameterization: we systematically vary the maximum strain weakening factor  $f_w^{\max}$  from 1 (no weakening) to 0.01 and the reference healing rate  $H_{660}$  in the range of  $10^{-14}$ - $10^{-16}$  s<sup>-1</sup>, which corresponds to  $\frac{1}{e}$  healing time scales of 3-300 Myr for the uppermost lower mantle. Finally, since these models including SW rheology show different final viscosity profiles, we select certain SW cases which we run again with an increased viscosity contrast between the upper and lower mantle ( $\lambda_{660} > 10$ ). The combined effect of such increased intrinsic lower-mantle viscosity and strain weakening behavior (lowering the lower mantle viscosity) gives more similar final viscosity profiles. As such, the effect of a changing Rayleigh number on mantle dynamics is eliminated and the direct effect of SW rheology can be determined.

### 261 3 Results

262 The relevant model parameters and output variables of all models run in this study  
 263 are summarized in Supporting Information Tables S1 and S2. Videos related to the cases  
 264 discussed in the text and/or highlighted in the figures can be found in the Supporting  
 265 Information related to this article. All models showcased in this study show plate-like  
 266 behavior according to the diagnostics of (Tackley, 2000b), and final average viscosity pro-  
 267 files of most models approximately agree with estimates from literature (see Support-  
 268 ing Information Fig. S4).

269 We first describe the evolution of our reference model (Section 3.1). In this model,  
 270 the strain field is tracked according to the newly-implemented finite strain approach with-  
 271 out the application of strain-dependent weakening or rheological healing. In Section (3.2),  
 272 we describe the effect of the implemented strain-weakening rheology on model behav-  
 273 ior. Two case studies are highlighted with various degrees of strain-weakening and rhe-  
 274 ological healing. Finally, in Section 3.3, we summarize the results of several case stud-  
 275 ies with various degrees of SW, but a similar final viscosity profile (Section 3.3).

#### 276 3.1 Reference model evolution

277 The temporal evolution of our reference model ( $M_0$ ), which does not include strain-  
 278 weakening, is shown in Fig. 3 and in Video S1. Soon after the start of model evolution,  
 279 the thermal boundary layers grow in amplitude, and after ample growth of boundary layer  
 280 instabilities, a mantle overturn initiates the onset of whole-mantle convection, after which  
 281 plate-tectonic behavior occurs (Table S1). The viscous flow associated with early model  
 282 dynamics (at 1.0 Gyr) causes a strain field in the lower mantle that is localized in re-  
 283 gions of buoyant, hot upwellings, and areas which are deflected by incoming, strong litho-  
 284 spheric drips/slabs (Fig. 3a). From the start of whole-mantle convection, the mantle grad-  
 285 ually cools and the frequent occurrence of active mantle plumes and subducting slabs

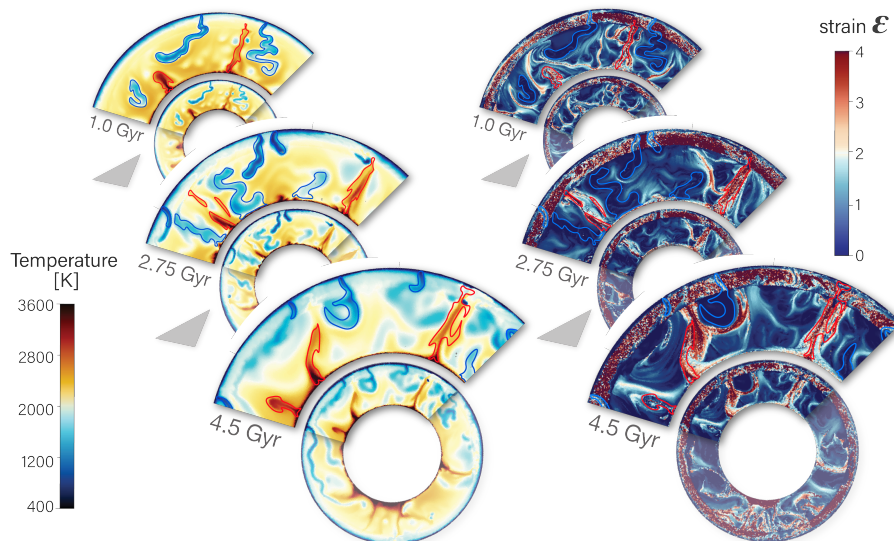


**Figure 3.** Temporal evolution of the reference model  $M_0$ , in which neither rheological healing nor rheological weakening is applied. Three snapshots of the temperature field (left) and strain field (right) are shown. Red outlines the edges of detected mantle plumes, and blue that of active downwellings (see Supporting Information Text S3 for their definitions).

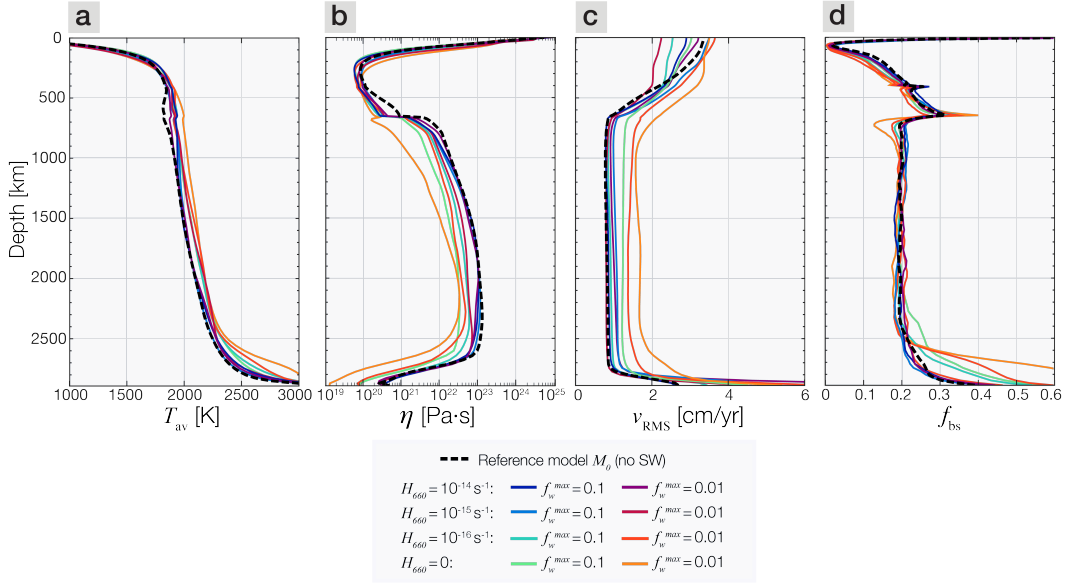


**Figure 4.** Radially averaged profiles of (a) temperature  $T$ , (b) viscosity  $\eta$ , (c) RMS velocity  $v_{\text{RMS}}$ , and (d) basalt fraction  $f_{\text{bs}}$  for all main models in this study. All radial profiles are averaged over time between 4.0 and 5.0 Gyr model time.

286 and active mantle plumes causes further complexity of the mantle strain pattern (Fig.  
 287 3). As the deformation history is reset at the 660 km boundary layer, small-scale strain  
 288 patterns in the upper mantle are not carried into the lower mantle. Instead, strain builds  
 289 up in downwelling (e.g., around slabs) and upwelling (plumes) regions of the lower man-  
 290 tle (Fig. 3).

291 The radially-averaged temperature profile displays the typical signal of efficient whole-  
 292 mantle convection with boundary layers superimposed on a mostly adiabatic geotherm  
 293 (Fig. 4a). The radial viscosity profile reflects the temperature- and depth-dependent rhe-  
 294 ology, as well as its compositional dependency expressed as a viscosity step towards higher  
 295 values from the upper- to lower mantle ( $\lambda_{660}$ ) (Fig. 4b). Mantle velocity is highest in  
 296 the bottom  $\sim 150$  km of the lower mantle and in the upper mantle (Fig. 4c). Finally, the  
 297 compositional profile shows efficient basalt segregation in a thin region on top of the CMB  
 298 (tens of km) and in the mantle-transition zone (Fig. 4d).

### 299 3.2 Influence of strain-dependent rheology

300 In this section, we separately describe the effects of SW rheology on several key as-  
 301 pects of mantle convection which were introduced in Section 1. First, the effect of SW  
 302 rheology on convective flow patterns is described (Section 3.2.1), followed by its effect  
 303 on the thermal evolution of the mantle (Section 3.2.2), on thermochemical piles forma-  
 304 tion (Section 3.2.3), and on the dynamics of mantle plumes (Section 3.2.4).

#### 305 3.2.1 Global mantle convective patterns

306 The radial profiles of viscosity and root mean-square (RMS) velocity of modelled  
 307 mantles (Fig. 4b-c), as well as their final averages (Fig. 5b-c) show clear trends for SW  
 308 rheology models. The average mantle viscosity is significantly lowered when SW rheol-  
 309 ogy is applied, mostly in the lower mantle (Fig. 4b). Final convective vigor ( $\sim v_{\text{RMS}}$ )  
 310 is increased for most SW models, also mainly accommodated in the lower(most) man-

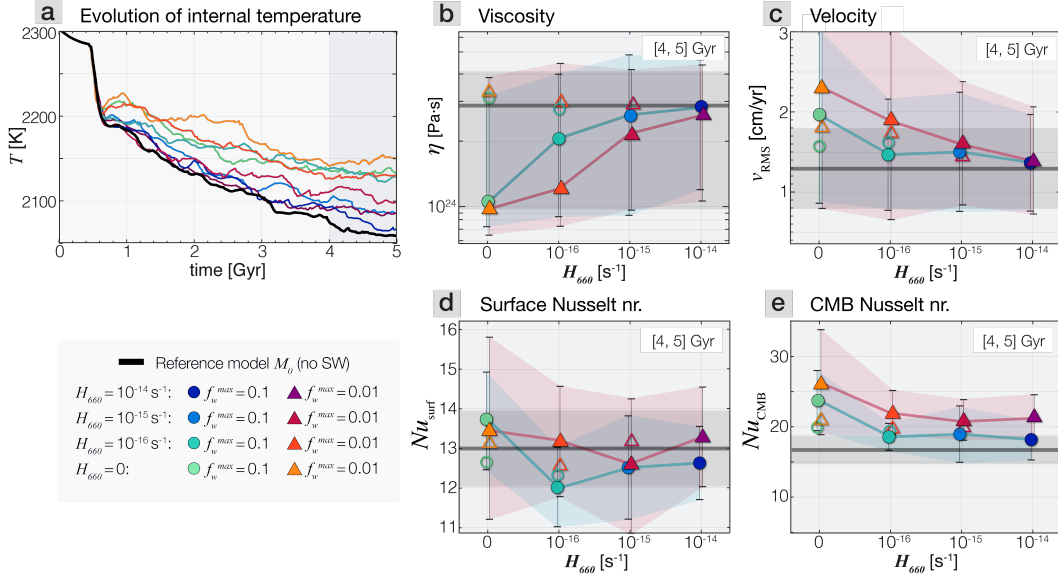


**Figure 5.** (a) Evolution of internal temperature for all main models, colors represent reference healing rate and applied weakening factor (see legend). (b)-(e) Selected output parameters (viscosity, velocity, surface and bottom  $Nu$  number) averaged between 4.0 and 5.0 Gyr of model time. The black line represents the reference model (neither strain-weakening nor rheological healing), with the gray shaded area showing the standard deviation. The horizontal axis represents the reference healing rate  $H_{660}$ , and the icon shape stands for the implemented strain-weakening factor  $f_w^{\max}$ . The error bars and colored shaded areas indicate the standard-deviation of the parameter over that time period. For selected cases, outline-only symbols are also plotted, which represent the results for the additional cases with an increased viscosity jump at the 660 km discontinuity (see Section 3.3 and Supporting Information Text S4).

311 tle (Fig. 4c) Figure 6 shows the detected mantle domain field, i.e., passive/active up -  
 312 and downwellings, of three selected models with variable degrees of SW rheology at  $\sim 4.5$   
 313 Gyr. It further shows the temporal evolution of the lateral distribution of this mantle  
 314 domain field at 1800 km depth (i.e., in the middle of the lower mantle). In comparison  
 315 to the reference model (Fig. 6a), SW models with an increased convective vigor show  
 316 a more chaotic planform of mantle flow (Fig. 6b,c) with a larger number of small plumes  
 317 present. The timescale of convection decreases with SW rheology as the convective vigor  
 318 increases (overturn time  $\tau \sim \frac{1}{v_{\text{RMS}}}$ , Miyagoshi et al. (2017)). The length-scale of con-  
 319 vection also decreases with SW rheology as the lower mantle consists of convection cells  
 320 with smaller aspect ratios, i.e., more narrow regions of up- and downwellings (Fig. 6b,c).  
 321 The temporal evolution shows that the upwelling plumes in the lower mantle have shorter  
 322 lifetimes than those in non-SW models. Figure 7a-c show the distribution of selected quan-  
 323 tities in the whole mantle domain for the same three models. The  $v_{\text{RMS}}$  histograms for  
 324 SW models are more skewed than that for the reference model, highlighting small do-  
 325 mains in the mantle with very high velocities. This highlights the (albeit small) domains  
 326 in which SW efficiently occurs. Interestingly, despite the changing pattern and vigor of  
 327 mantle flow (described above), the statistical distribution of the age of mantle materi-  
 328 als (defined by the time since a tracer last underwent a melting episode) in the whole  
 329 mantle is similar for cases with and without SW (right panels of Fig. 7).

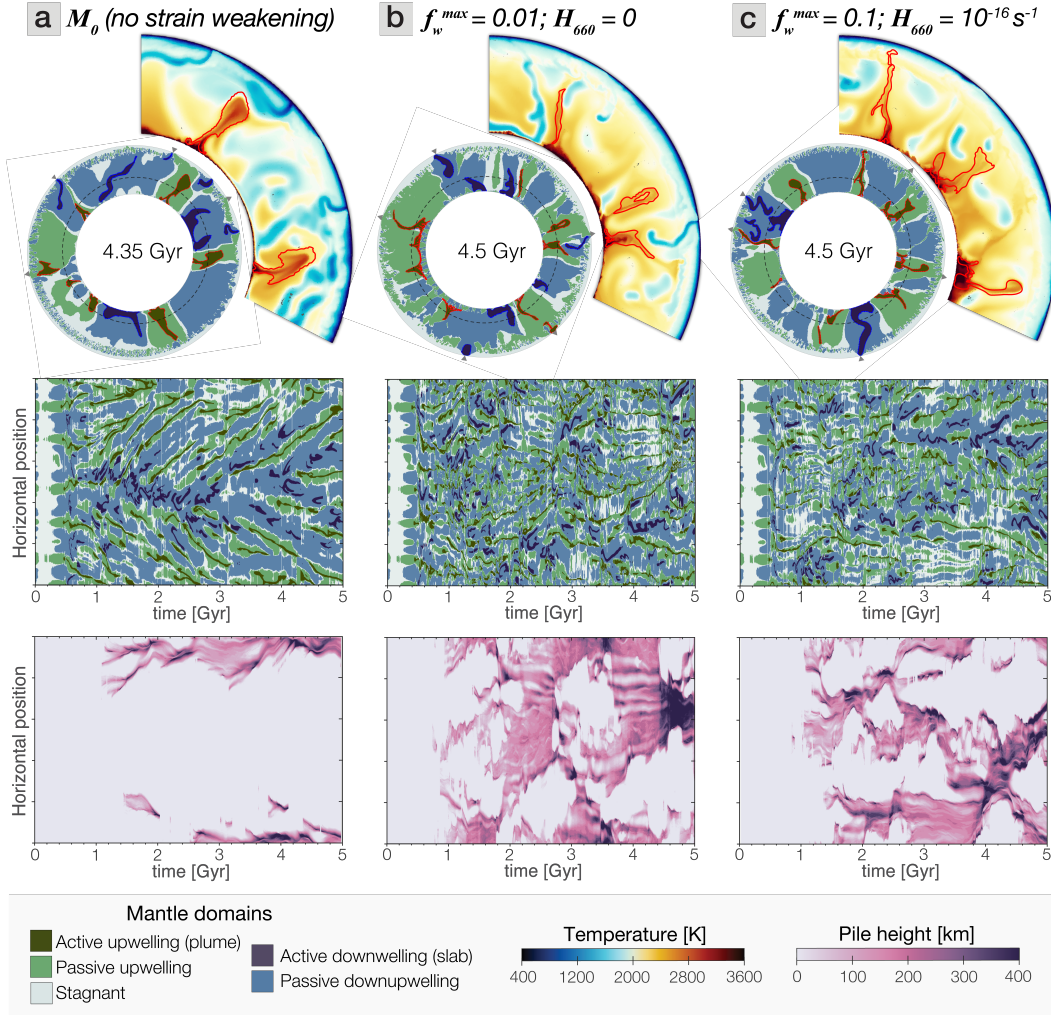


**Figure 6.** Top: age-of-the-Earth snapshots for three selected models showing the mantle domain field and the temperature field (a zoom-in for part of the mantle domain). Middle: temporal evolution of the lateral distribution of this field at 1800 km depth. Red outline: active mantle upwellings, blue outline: active mantle downwellings. See Section 2.5 for the definitions of the mantle domains. Bottom: temporal evolution of the lateral distribution of detected thermochemical piles atop the core-mantle boundary, color-coded according to the height of the detected pile. (a) Reference model: neither SW rheology nor rheological healing, (b) extreme case of strong strain-weakening and no rheological healing, and (c) model with SW rheology and healing simultaneously activated.

330

### 3.2.2 Thermal evolution

331

332

333

334

335

336

337

In models with SW rheology, the mantle cools down to higher final equilibrium mantle temperatures than in models with less or no SW rheology (Figs. 5a and 4c). Even with a high healing rate of  $H_{660} = 10^{-14} \text{ s}^{-1}$ , which causes strain in the lower mantle to heal on short geological timescales (Text S2), higher final internal temperatures are reached. This is also apparent by the relation between top and bottom Nusselt number ( $Nu_{\text{top}}$  and  $Nu_{\text{bot}}$ ).  $Nu_{\text{top}}$  is not much affected by strain-weakening rheology, while  $Nu_{\text{bot}}$  is on average significantly higher for SW models (Fig. 5 d). The ratio of top/bottom

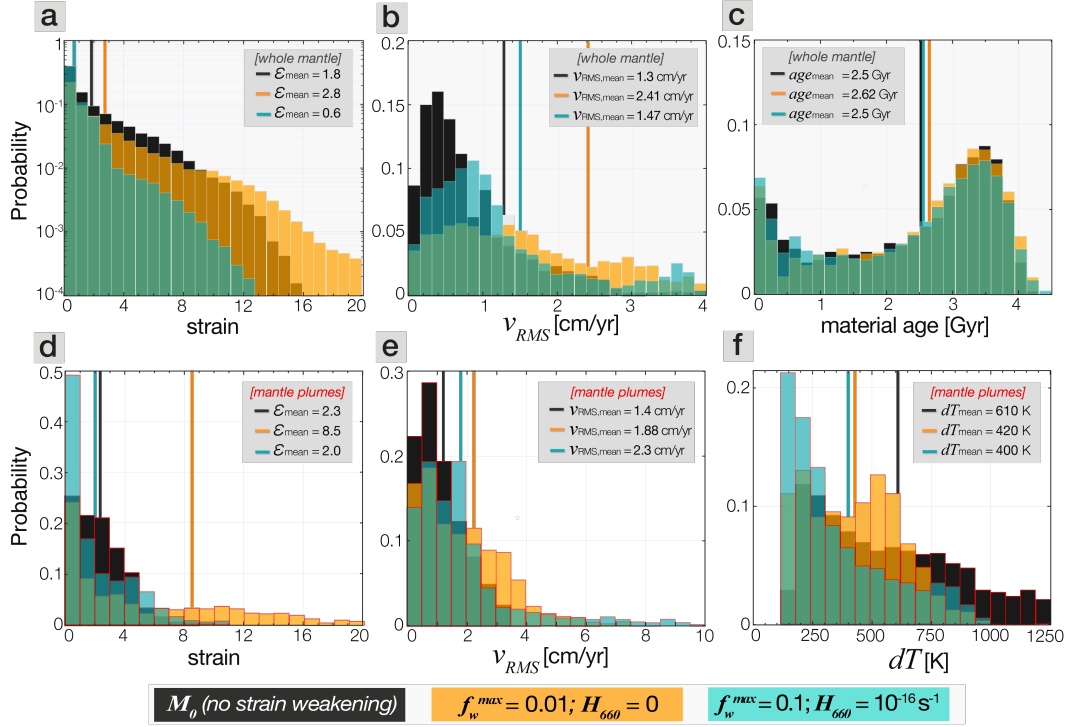


**Figure 7.** Histograms of selected quantities for selected models (color scale), averaged between 4.0 and 5.0 Gyr of model time. (a)-(c) show the distribution of the strain field ( $\epsilon$ ), the root mean-square velocity ( $v_{RMS}$ ), and the material age ( $age$ ) within the whole mantle domain. (d)-(f) show the distribution of the strain field ( $\epsilon$ ), the root mean-square velocity ( $v_{RMS}$ ), and the average horizontal temperature anomaly of the material ( $dT$ ) within the detected active mantle upwellings (plumes). The vertical lines represent the mean values for each histogram. Note the vertical axis of the strain histogram in panel (a) is logarithmic, whereas that in panel (d) is not.

338 Nusselt number is thus lowered for SW models throughout their evolution. This implies  
 339 that heat is more efficiently removed from the core. In our models (constant tem-  
 340 perature), this causes a higher final mantle temperature in models in which SW rheol-  
 341 ogy is applied. How our assumption of constant core temperature may affect these re-  
 342 sults is discussed in Section 4.4.

### 343 3.2.3 Formation of piles

344 Basalt segregation is most efficient in models with strong SW, because these mod-  
 345 els exhibit a low-viscosity, high-temperature mantle (see above and Figs. 4d, and Videos).  
 346 Due to efficient segregation in these models, basaltic material tends to settle more ef-  
 347 ficiently in the lowermost mantle, stabilizing the formation of large thermochemical piles  
 348 that cover more of the CMB (Fig. 6; Table S1). Also, the transition zone (410-660 km  
 349 depth) becomes more enhanced in basaltic material ( $f_{bs} \approx 40\%$ ), while the regions around  
 350 it are more depleted (Figs. 4d) (as in e.g. Ogawa, 2003; Nakagawa & Buffett, 2005; Davies,  
 351 2008; Yan et al., 2020). Moreover, the thermochemical piles are internally convecting in  
 352 SW models, affecting overall heat fluxes through the mantle: due to the high intrinsic  
 353 pile density, heat can build up within the piles, forming another thermal boundary layer

354 on top of them. Thus, these piles can act as plume generation zones in the models as ac-  
 355 tive upwellings sporadically form on top of them, as well as along their edges.

### 356 **3.2.4 Plume dynamics**

357 Strain mainly localizes in hot upwellings, where material is deformed soon after model  
 358 onset and subsequently subjected to weakening. Even though rheological healing par-  
 359 tially limits such strain localisation, plume channels are still weakened in the presence  
 360 of healing (see Supporting Information Text S2 and Fig. S3). According to classical ther-  
 361 mal plume formation theories (e.g., Howard, 1964), the temperature and width of a man-  
 362 tle plume is related to the time over which the boundary layer grows. A thermal insta-  
 363 bility occurs when the critical boundary layer Rayleigh number is reached ( $Ra_{\text{local}} =$   
 364  $Ra_{\text{local,crit}}$ ) (Howard, 1964). If the viscosity of the material is large (low  $Ra_{\text{local}}$ ), longer  
 365 onset times occur, i.e., the growth rate of the instability depends inversely on the local  
 366 viscosity (e.g., Howard, 1964; Griffiths & Campbell, 1990; Olson, 1990). Hot anomalies  
 367 begin to separate from the layer as soon as their speed of buoyant ascent exceeds their  
 368 growth rate. In our SW models, the lower viscosity of weakened plume materials would,  
 369 according to the theory above, decrease the onset times of the instabilities. Since these  
 370 SW instabilities have had less time to grow, there is a smaller temperature build-up com-  
 371 pared to non-SW thermal instabilities. This precludes the growth of a wider, anomalously  
 372 hot mantle plume with mushroom-shaped heads as seen in our reference model (Fig. 6a).  
 373 Instead, only a narrow conduit at the center of the weakened channel remains anoma-  
 374 lously hot, while a wider (and less hot) conduit transfers material upward. This absence  
 375 of mushroom-shaped plume heads is evident for weakened plumes in both pure SW cases  
 376 as well as SW + rheological healing models (Fig. 6b-c and Videos S2-S3).

377 The positive feedback between weakening and strain localization causes a low-viscosity  
 378 channel to form in and around plumes, allowing for rapid transport of mass and heat from  
 379 depth towards the surface. The typical velocities in the plume conduit tend to increase  
 380 for more efficient SW (i.e., for lower  $f_w^{\text{max}}$  or lower  $H_{660}$ ), while the excess temperatures  
 381 are lower for more efficient SW (Fig. 7, Table S2). These distinct plume dynamics caused  
 382 by SW rheology are further apparent in the bottom Nusselt number ( $Nu_{\text{bot}}$ ). Final  $Nu_{\text{bot}}$   
 383 is, on average, higher for models with most efficient SW rheology, linked to the thinner  
 384 thermal boundary layers and higher boundary layer Rayleigh numbers (Fig. 5f). This  
 385 implies that heat is more effectively lost by convection (i.e., via mantle plumes) rather  
 386 than conduction. The weakened conduits are easily deflected by background flow or by  
 387 incoming slabs (see Video S1). Typical timescales of plume lifetimes decrease from  $\sim 500$ –  
 388  $1000$  Myr for the reference case to few 100 Myrs for the extreme SW cases (lower pan-  
 389 els in Fig. 6).

### 390 **3.3 Influence of mantle viscosity profile**

391 Each model discussed above displays a distinct effective viscosity profile through  
 392 time (Fig. 4), which, in turn, controls convective vigor and thereby strongly affects model  
 393 evolution. In order to distinguish the direct (first-order) effects of SW rheology on man-  
 394 tle dynamics from the indirect effects of SW rheology through the radial viscosity pro-  
 395 file (second-order), we explore additional SW cases with a higher intrinsic viscosity jump  
 396 at 660 km depth ( $\lambda_{660}$ ), such that the final viscosity profile is similar to that of the re-  
 397 ference case. A detailed description of these results is given in Supporting Information  
 398 Text S4. As a summary, these additional cases show a similar average convective vigor  
 399 and thermal evolution as the reference case due to their similar viscosity profile. How-  
 400 ever, plume dynamics and the size of thermochemical piles are still affected in the same  
 401 way as in the previously described SW models (see Supporting Information Text S4 and  
 402 Figs. S5, S6). In fact, the localization of increased flow velocity in the narrow upwelling  
 403 mantle plumes is even significantly more pronounced in these additional SW models. More-  
 404 over, thermochemical piles in the additional SW models are still substantially larger. Hence,

we conclude that SW rheology is the critical ingredient for the weakening of plume channels, their narrow shapes and relatively low thermal anomalies, as well as the formation and stabilization of large thermochemical piles. Second-order effects, such as the higher final mantle temperature, and the significantly higher average mantle flow velocities, are caused by the modification of the viscosity profile through SW.

## 4 Discussion

### 4.1 Mantle mixing and geochemical reservoirs

With an increasing convective vigor and decreasing length-scale of convection for SW models (Figs. 6 and S6), one might expect the timescale of mantle material mixing to decrease (e.g., Coltice & Schmalzl, 2006). However, in high convective-vigor SW models, basalt more easily segregates from harzburgite and thermochemical piles, which are in turn more stable over time (Section 3.2.3). Such a relation between lower mantle viscosity and more efficient basalt segregation is consistent with other studies (e.g., Yan et al., 2020). Hence, heterogeneity mixing turns out to be less efficient in models with SW rheology. Yet, the statistical distribution of mantle material age in the whole mantle is similar for all cases (Figs. 7c and S7). While a slightly higher proportion of very ancient material ( $>4$  Ga) is preserved in SW models, a significant part of this material portion is accommodated in the thermochemical piles, which are larger and more stable in SW models. The similarity of preservation in all our models, and particularly in the convecting mantle, is contrary to earlier suggestions that SW can promote the survival of primordial materials (e.g., Girard et al., 2016; Chen, 2016). In our SW models, convection patterns are not critically stabilized over time. This result may be attributed to the lack of strain weakening in downwelling regions. Only if both upwellings and downwellings were significantly weaker than the regions in-between, we would expect efficient preservation in these in-between regions (Ballmer et al., 2017; Gülcher et al., 2020). For example, it has been proposed that grain-size reduction in cold slabs that enter the lower mantle causes local weakening (Ito & Sato, 1991; Karato et al., 2001; Yamazaki et al., 2005; Dannberg et al., 2017). Such grain-reduction weakening in combination with SW plumes may cause a style of convection dynamics more akin to previously proposed (Fig. 1b), with weakening occurring in both downwelling slabs and upwelling plumes. Future work should test if this is indeed the case.

### 4.2 Planetary interior evolution

Since SW rheology in the lower mantle affects CMB heat fluxes and their ratio to surface heat fluxes (Fig. 5, Table S1), it may have a substantial control on core dynamics as well as mantle cooling rates. The heat transfer from the core into the base of the mantle greatly affects the sustainability of a planetary dynamo through its control on the vigor of core convection, and the onset of inner core crystallization (Stevenson, 2003; Lay et al., 2008). Moreover, the spatial pattern of (geo-)magnetic secular variations is commonly attributed to changes in CMB heat fluxes and mantle plumes (e.g., Larson & Olson, 1991; Courtillot & Olson, 2007; Biggin et al., 2012).

Modern estimates of CMB heat flux for the Earth range from several TW up to 15 TW (e.g., Lay et al., 2008; Nakagawa, 2020), i.e., significantly lower than outcomes in our numerical models (Table S1). However, these estimates may be underestimated since they do not consider additional CMB heat flux by advection due to cold plumes (subducted plates) arriving at the base of the mantle (Labrosse, 2002). Moreover, we do not explicitly account for thermal evolution in our models (constant core temperature of 4000 K and absence of internal heating), and therefore early CMB heat flow is likely underestimated and present-day heat flux overestimated. Nevertheless, in our models, mantles with SW rheology pull out heat more efficiently from the core, which would alter planetary thermal evolution. It must be noted that if core cooling would be combined

455 with SW rheology, the core would cool faster which, in turn, would lower CMB heat flux  
 456 and possibly final mantle temperatures. Future studies should investigate the combined  
 457 effect of SW rheology and core cooling, and assess whether the indirect SW rheology ef-  
 458 fect of increasing mantle temperatures (only minor when comparing models with sim-  
 459 ilar viscosity structures, see Section 3.3) still holds.

460 The relevance of SW rheology for (exo-)planets depends on their mineralogy and  
 461 internal structure. Stars in the solar neighborhood show diverse Mg-Fe-Si compositions  
 462 (Hinkel et al., 2014), with the solar composition being average in terms of Mg/Si, and  
 463 near the high end of Fe/Mg (Asplund et al., 2009). Assuming stellar compositions as a  
 464 proxy for rocky planet compositions (as in Spaargaren et al., 2020), planets in stellar sys-  
 465 tems with  $\text{Mg/Si} < 1$  likely have no ferropericase in their mantle, hence no strain weak-  
 466 ening is expected to occur. Rocky planets associated with  $\text{Mg/Si} \gg 1.5$  stars feature sig-  
 467 nificant amounts of mantle ferropericase, hence the material would already be weak at  
 468 very small (or even zero) strain. The majority of rocky exoplanets should have an Earth-  
 469 like bulk composition with  $1 < \text{Mg/Si} \leq 1.5$  (e.g., Spaargaren et al., 2020), where SW rhe-  
 470 ology potentially occurs in the mantle. Moreover, a recent study established the stabil-  
 471 ity of a very weak B2-(Mg,Fe)O phase under extreme pressures (Coppari et al., 2021),  
 472 which may dramatically affect the deep mantle rheology of Super Earths, potentially pro-  
 473 moting SW.

### 474 4.3 Thermochemical piles

475 The current degree-2 pattern of Earth’s mantle flow, anchored by the two antipodal  
 476 LLSVP piles (Dziewonski et al., 2010), has been suggested to be a stable energy con-  
 477 figuration from the point of view of Earth’s moment of inertia and to exist for at least  
 478 200 Myrs (Burke et al., 2008; Torsvik et al., 2010, 2014; Conrad et al., 2013). Yet, this  
 479 configuration is only energetically stable if LLSVPs are (much) denser than slabs, which  
 480 is yet unclear (Koelemeijer et al., 2017a, 2017b; McNamara, 2019). The intrinsic high  
 481 density of recycled crustal materials (basalt) already causes piles to form in our mod-  
 482 els (Fig. 6), in agreement with various geodynamical studies (Nakagawa & Buffett, 2005;  
 483 Nakagawa et al., 2010; Tackley, 2012; Y. Li et al., 2014). Here, we show how SW rhe-  
 484 ology causes more efficient basalt segregation, and the formation of larger, multiple piles  
 485 that cover a larger extend of the CMB (see Fig. 6 and Supporting Information Table S1).

486 Such thermochemical piles can act as a thermal insulator of part of the heat com-  
 487 ing from the CMB (e.g., Lay et al., 2008; Nakagawa, 2020). Yet, the overall CMB heat  
 488 flux is increased in SW rheology models. These increased values are accommodated by  
 489 the much larger fluxes within the weakened plume channels (Supporting Information Ta-  
 490 ble S2) as well as small-scale convective fluxes within the piles (see e.g., Fig. 6b). More-  
 491 over, plumes formed from this (secondary) thermal boundary layer have by default less  
 492 heat available (Farnetani, 1997), since the temperature difference between the piles and  
 493 ambient mantle is less than that between the adiabat and the CMB. This could partially  
 494 explain lower temperature anomalies of these mantle plumes, although note that weak-  
 495 ened plumes not only rise from the piles, but also from the CMB (see Figs. 6, S6, and  
 496 Videos S2-S5).

### 497 4.4 Plume formation

498 As described in the results section (3.2.4), the differences in plume dynamics be-  
 499 tween our numerical models agree with scalings and relationships found in early classi-  
 500 cal thermal plume formation theories (e.g., Howard, 1964; Griffiths & Campbell, 1990;  
 501 Olson, 1990). Thermochemical plumes, on the other hand, have different compositions,  
 502 shapes and, ascent styles, as buoyancy forces of the plume are additionally affected by  
 503 rheological and chemical density contrasts (Farnetani & Samuel, 2005; Davaille & Vat-  
 504 terville, 2005; Lin & Van Keken, 2006). Thermochemical plumes consisting of intrinsi-

505 cally dense material are generally wider than purely thermal plumes due to dense ma-  
 506 terial that sinks back into the ascending plume (Davaille & Vatteville, 2005). Plumes in  
 507 our models are of thermochemical origin, yet weakened thermochemical plume conduits  
 508 are still narrow for SW rheology models.

509 The morphology of fully developed thermal plumes in the mantle is governed by  
 510 the viscosity contrast between the plume and the mantle, and the interaction with the  
 511 background mantle flow through which the plume ascends (Whitehead & Luther, 1975).  
 512 The classical plume model includes a broad plume head, up to roughly thousand km in  
 513 diameter, followed by a narrow plume tail, not wider than a couple of hundred kilome-  
 514 ters (Richards et al., 1989; Sleep, 1990; Griffiths & Campbell, 1990; Davaille, 1999). In  
 515 our models, plumes weakened by SW rheology substantially differ from the classical head-  
 516 and-tail plume structure. Weakening of narrow conduit provides a pathway (lubrication  
 517 channel) through which hot material can readily rise. In such weakened plume conduits,  
 518 transport of mass and heat occurs more efficiently. Moreover, as relatively little ther-  
 519 mal buoyancy needs to be built up to drive the plume, no head-and-tail geometry is formed.  
 520 Indeed, a number of studies have shown that the conduit radius is proportional to  $\eta^{1/4}$ ,  
 521 where  $\eta$  is the viscosity of the hot thermal boundary layer (Griffiths & Campbell, 1990;  
 522 Olson et al., 1993). Such narrow weakened plume conduits have a shorter lifetime than  
 523 non-weakened plumes (Fig. 6) and they can be more easily diverted by large-scale mo-  
 524 tions and rheological contrasts in the mantle, as can be seen in the supplementary Videos.

#### 525 4.5 Mantle plumes on Earth

526 On Earth, the mismatch between lower mantle and core adiabats implies a super-  
 527 adiabatic temperature jump across the CMB of about 1000-1500 K (Jeanloz & Morris,  
 528 1986; Boehler, 1996; Lay et al., 2008). Most mantle plumes on Earth, however, are in-  
 529 ferred to have excess temperatures of only 100-300 K (e.g., Albers & Christensen, 1996).  
 530 Even when extrapolating such excess temperatures to the lower mantle, temperature anoma-  
 531 lies of about 500 K have been inferred at the CMB (Albers & Christensen, 1996), still  
 532 lower than the expected boundary layer temperature difference (Boehler, 1996). It has  
 533 been argued that this mismatch is an indication for plumes rising from the top of a com-  
 534 positionally distinct layer at the base of the mantle (Farnetani, 1997) or for super-adiabatic  
 535 rise of plumes (Bunge, 2005). Strain-weakening rheology of lower mantle materials could  
 536 additionally help to explain the discrepancy between expected thermal anomalies and  
 537 observed thermal anomalies of deep-seated mantle plumes, via the shorter onset times  
 538 of thermal instabilities (see Section 3.2.4). On Earth, many deep-sourced plumes  
 539 are thought to ascend within a few tens of million years to the base of the lithosphere  
 540 (e.g., Torsvik et al., 2021). From our modelled mantle plume upwelling velocities, pre-  
 541 dicted average ascent times are reduced from  $\sim 200$  Myr (for non-SW models) to an  $\sim 110$   
 542 Myr (with strain-weakening rheology). The fastest plumes in our SW models have as-  
 543 cent times of only 30 Myr (for 8 cm/yr rising speed), in contrast to 70 Myr for the fastest  
 544 non-weakened plumes. Therefore, SW rheology could help to explain mantle plume rise  
 545 speeds in the Earth's mantle. An alternative explanations for fast plume ascent involves  
 546 stress-dependent non-Newtonian rheology in the lower mantle (van Keken, 1997), which  
 547 is argued to produce significantly reduced plume ascent times - although in combination  
 548 with larger temperature excesses because of the faster travel time (van Keken, 1997), which  
 549 is not the case for weakened plumes in this study.

550 Even though LLSVPs have been commonly linked to plume generation (e.g., Torsvik  
 551 et al., 2010), this link remains controversial. French and Romanowicz (2015) used whole-  
 552 mantle seismic imaging techniques to argue for the presence of broad (not thin), quasi-  
 553 vertical plumes (i.e.,  $\sim 1000$  km in width) beneath many prominent hotspots. The broad  
 554 plumes were inferred to be thermochemical of origin and root at the base of the man-  
 555 tle in patches of greatly reduced shear velocity (e.g., LLSVPs). Another line of thought  
 556 is that the same seismic structures are actually a collection of poorly-resolved narrow

557 mantle plumes (Schubert et al., 2004; Davaille & Vatteville, 2005; Davaille & Romanow-  
 558 icz, 2020). In this scenario, LLSVPs are composed of plume clusters rather than being  
 559 made up of stable, wide thermochemical piles with broad plume structures atop (as ar-  
 560 gued by French & Romanowicz, 2015). With state-of-the-art seismic methods, narrow  
 561 mantle plumes are difficult - even impossible - to be uniquely distinguished (e.g. Hwang  
 562 et al., 2011); hence further methodological advances are needed to convincingly discrim-  
 563 inate between these two scenarios. In our models, SW rheology promotes the existence  
 564 of multiple weak plume channels, that could possibly be imaged as plume clusters. Yet,  
 565 in contrast to the plume bundle hypothesis (Schubert et al., 2004; Davaille & Romanow-  
 566 icz, 2020), such narrow, weakened plumes occur in combination with stable, thermochem-  
 567 ical piles in the lowermost mantle. SW rheology could also help to explain faint seismi-  
 568 cally slow anomalies - or even the absence of detectable anomalies - beneath several hotspots,  
 569 such as Louisville, Galapagos, and Easter (Pacific) (Davaille & Romanowicz, 2020). Fi-  
 570 nally, it must be noted that time-dependency is a key factor when interpreting present-  
 571 day tomographic images of mantle upwellings. The classical image of a conduit rising  
 572 from the CMB all the way to the lithosphere is only valid during part of the plume’s life-  
 573 time (Davaille & Vatteville, 2005). Therefore, plumes might not be easy to detect in to-  
 574 mographic images, particularly if they are weakened by SW rheology, and/or deflected  
 575 by mantle flow.

#### 576 **4.6 Future studies**

577 Several future scientific avenues may be carried out to advance this study on the  
 578 effect of SW rheology on mantle dynamics. First of all, future studies could advance our  
 579 implementation by making the SW rheology composition-dependent, causing strain-dependent  
 580 weakening to mainly occur in ferropiclasite-enhanced regions. Subducted oceanic crust  
 581 at lower mantle conditions does not contain any ferropiclasite, but instead, contains much  
 582 cubic  $\text{CaSiO}_3$  perovskite (Hirose, Sinmyo, & Hernlund, 2017; Wicks & Duffy, 2016; Tschauner  
 583 et al., 2021), which may be intrinsically weak. It is further interesting to test this composition-  
 584 dependent weakening in combination with the existence of ancient bridgmanite-enhanced  
 585 regions in the mid-mantle (as in Gülcher et al., 2020, 2021), which should not exhibit  
 586 SW due to the absence of ferropiclasite, hence promoting their preservation. Moreover,  
 587 it remains to be explored how strain-dependent and grain size-dependent rheology in-  
 588 teract with each other in the lower mantle (see Section 4.1). Finally, with the tracking  
 589 of the deformation matrix in full tensor form, additional work can focus on the direction-  
 590 dependency of the strain ellipse and weakening behavior and their effects on whole-mantle  
 591 dynamics.

## 592 **5 Conclusions**

- 593 • We implemented a new strain-dependent rheology for lower mantle materials, com-  
 594 bining rheological weakening and healing, in numerical models of global-scale man-  
 595 tle convection.
- 596 • Strain particularly focuses in anomalously hot regions, such as piles atop the CMB  
 597 and hot mantle plumes, also when rheological healing is applied.
- 598 • SW rheology is the key ingredient for the weakening of plume channels as well as  
 599 forming large thermochemical piles
- 600 • Second-order effects of SW rheology, caused by the changing mantle dynamics due  
 601 to a reduction of viscosity in the lower mantle, are higher equilibrium mantle tem-  
 602 peratures and the significantly higher average mantle flow velocities.
- 603 • Weakened mantle plumes form narrow lubrication channels in the mantle through  
 604 which hot material readily rises, and they have shorter lifetimes.
- 605 • This new kind of plume dynamics may explain moderate plume excess temper-  
 606 atures beneath hotspots (only up to 200–300 K), given the much larger temper-  
 607 ature difference across the core–mantle boundary ( $\sim 1000$  K).

## 608 Acronyms

609 **Myr** million year  
 610 **Gyr** billion year  
 611 **LBF** load-bearing framework  
 612 **IWL** interconnected weak layers  
 613 **CMB** core-mantle boundary  
 614 **LLSVP** large low shear-wave velocity province  
 615 **SW** strain-weakening

## 616 Open Research

617 The open-source StagLab toolbox (Cramer, 2018) was used for detecting differ-  
 618 ent mantle domains in the numerical models, creation of histogram data (Figs. 6-7, S6-  
 619 S7), and creating the Videos S1-S5. The new mantle domain detection scheme (as dis-  
 620 cussed in Supporting Information Text S3) is implemented in a STAGLAB 6.0 version,  
 621 and it is available on <https://github.com/annaguelcher/StagLab-OS.git>. Moreover, the  
 622 open-source Python module StagPy (<https://stagpy.readthedocs.io/en/stable/>, last ac-  
 623 cess: 17 July 2021) was also used for post-processing of the numerical data and produc-  
 624 tion of radial and temporal profiles (Figs. 4, 5, S2, S4, and S5). The numerical code is  
 625 available by reasonable request to Paul J. Tackley. All the data corresponding to the nu-  
 626 merical experiments of this paper are too large to be placed online, but they can be re-  
 627 quested from the corresponding author (Anna J. P. Gülcher), as can the input files for  
 628 all model runs.

## 629 Supporting Information

- 630 1. Text S1 to S4
- 631 2. Figures S1 to S7
- 632 3. Tables S1 and S2
- 633 4. Videos S1 to S5

## 634 Acknowledgments

635 This research has mainly been supported by the ETH Zürich Research Commission (grant  
 636 no. ETH-33 16-1). M. T. was supported by the Bayerisches Geoinstitut Visitor’s Pro-  
 637 gram. We thank Lukas Fuchs for helpful discussions related to this work, and Fabio Cramer  
 638 for discussions related to visualisations and color maps. All numerical simulations were  
 639 performed on ETH Zürich’s Euler cluster. For 2D visualisation of the models, we used  
 640 the open-source software ParaView (<http://paraview.org>, last access: 2 September 2021).  
 641 Several perceptually uniform scientific color maps (Cramer, 2018, <https://doi.org/10.5281/zenodo.1243862>)  
 642 were used to prevent visual distortion of the figures.

## 643 References

- 644 Albers, M., & Christensen, U. R. (1996). The excess temperature of plumes rising  
 645 from the core-mantle boundary. *Geophysical Research Letters*, *23*(24), 3567–  
 646 3570. doi: 10.1029/96GL03311
- 647 Ammann, M. W., Brodholt, J. P., Wookey, J., & Dobson, D. P. (2010). First-  
 648 principles constraints on diffusion in lower-mantle minerals and a weak D”  
 649 layer. *Nature*, *465*(7297), 462–465. Retrieved from [http://dx.doi.org/](http://dx.doi.org/10.1038/nature09052)  
 650 [10.1038/nature09052](http://dx.doi.org/10.1038/nature09052) doi: 10.1038/nature09052
- 651 Asplund, M., Grevesse, N., Sauval, A. J., & Scott, P. (2009). The chemical compo-

- sition of the sun. *Annual Review of Astronomy and Astrophysics*, *47*, 481–522. doi: 10.1146/annurev.astro.46.060407.145222
- Ballmer, M. D., Houser, C., Hernlund, J. W., Wentzcovitch, R. M., & Hirose, K. (2017). Persistence of strong silica-enriched domains in the Earth’s lower mantle. *Nature Geoscience*, *10*(3), 236–240. doi: 10.1038/ngeo2898
- Biggin, A. J., Steinberger, B., Aubert, J., Suttie, N., Holme, R., Torsvik, T. H., ... Van Hinsbergen, D. J. (2012). Possible links between long-term geomagnetic variations and whole-mantle convection processes. *Nature Geoscience*, *5*(8), 526–533. doi: 10.1038/ngeo1521
- Boehler, R. (1996). Melting temperature of the Earth’s mantle and core: Earth’s thermal structure. *Annual Review of Earth and Planetary Sciences*, *24*, 15–40. doi: 10.1146/annurev.earth.24.1.15
- Bunge, H. P. (2005). Low plume excess temperature and high core heat flux inferred from non-adiabatic geotherms in internally heated mantle circulation models. *Physics of the Earth and Planetary Interiors*, *153*(1-3), 3–10. doi: 10.1016/j.pepi.2005.03.017
- Burke, K., Steinberger, B., Torsvik, T. H., & Smethurst, M. A. (2008). Plume Generation Zones at the margins of Large Low Shear Velocity Provinces on the core-mantle boundary. *Earth and Planetary Science Letters*, *265*(1-2), 49–60. doi: 10.1016/j.epsl.2007.09.042
- Chen, J. (2016). Lower-mantle materials under pressure. *Science*, *351*(6269), 122–123. doi: 10.1126/science.aad7813
- Christensen, U. R., & Hofmann, A. W. (1994). Segregation of subducted oceanic crust in the convecting mantle. *Journal of Geophysical Research*, *99*(B10), 19,867–19,884. doi: 10.1029/93jb03403
- Čížková, H., van den Berg, A. P., Spakman, W., & Matyska, C. (2012). The viscosity of Earth’s lower mantle inferred from sinking speed of subducted lithosphere. *Physics of the Earth and Planetary Interiors*, *200-201*, 56–62. doi: 10.1016/j.pepi.2012.02.010
- Coltice, N., & Schmalzl, J. (2006). Mixing times in the mantle of the early Earth derived from 2-D and 3-D numerical simulations of convection. *Geophysical Research Letters*, *33*(23), 5–8. doi: 10.1029/2006GL027707
- Conrad, C. P., Steinberger, B., & Torsvik, T. H. (2013). Stability of active mantle upwelling revealed by net characteristics of plate tectonics - supplementary. *Nature*, *498*, 479–482. doi: 10.1038/nature
- Coppari, F., Smith, R. F., Wang, J., Millot, M., Kim, D., Rygg, J. R., ... Duffy, T. S. (2021). Implications of the iron oxide phase transition on the interiors of rocky exoplanets. *Nature Geoscience*, *14*(3), 121–126. Retrieved from <http://dx.doi.org/10.1038/s41561-020-00684-y> doi: 10.1038/s41561-020-00684-y
- Courtillot, V., & Olson, P. (2007). Mantle plumes link magnetic superchrons to phanerozoic mass depletion events. *Earth and Planetary Science Letters*, *260*(3-4), 495–504. doi: 10.1016/j.epsl.2007.06.003
- Crameri, F. (2018). Geodynamic diagnostics, scientific visualisation and StagLab 3.0. *Geoscientific Model Development*, *11*(6), 2541–2562. doi: 10.5194/gmd-11-2541-2018
- Crameri, F., & Tackley, P. J. (2014). Spontaneous development of arcuate single-sided subduction in global 3-D mantle convection models with a free surface. *Journal of Geophysical Research: Solid Earth*, *119*(7), 5921–5942. doi: 10.1002/2014JB010939
- Dannberg, J., Eilon, Z., Faul, U., Gasmöller, R., Moulik, P., & Myhill, R. (2017). The importance of grain size to mantle dynamics and seismological observations. *Geochemistry Geophysics Geosystems*, *18*, 3034–3061. Retrieved from 10.1002/2016GC006787 doi: 10.1002/2017GC006944.Received
- Davaille, A. (1999). Two-layer thermal convection in miscible viscous fluids. *Journal*

- 707 *of Fluid Mechanics*, 379, 223–253. doi: 10.1017/S0022112098003322
- 708 Davaille, A., & Romanowicz, B. (2020). Deflating the LLSVPs: Bundles of Man-  
709 tle Thermochemical Plumes Rather Than Thick Stagnant “Piles”. *Tectonics*,  
710 39(10), 1–21. doi: 10.1029/2020TC006265
- 711 Davaille, A., & Vatteville, J. (2005). On the transient nature of mantle plumes. *Geo-  
712 physical Research Letters*, 32(14), 1–4. doi: 10.1029/2005GL023029
- 713 Davies, G. F. (2007). Thermal Evolution of the Mantle. *Treatise on Geophysics*, 9,  
714 197–216. doi: 10.1016/B978-044452748-6.00145-0
- 715 Davies, G. F. (2008). Episodic layering of the early mantle by the ‘basalt barrier’  
716 mechanism. *Earth and Planetary Science Letters*, 275(3-4), 382–392. doi: 10  
717 .1016/j.epsl.2008.08.036
- 718 de Montserrat, A., Faccenda, M., & Pennacchioni, G. (2021). Extrinsic Anisotropy  
719 of Two-Phase Newtonian Aggregates : Fabric Characterization and Parameter-  
720 ization. *Journal of Geophysical Research: Solid Earth*, 126(e2021JB022232).
- 721 Dziewonski, A. M., Lekic, V., & Romanowicz, B. A. (2010). Mantle Anchor Struc-  
722 ture: An argument for bottom up tectonics. *Earth and Planetary Science Let-  
723 ters*, 299(1-2), 69–79. doi: 10.1016/j.epsl.2010.08.013
- 724 Farnetani, C. G. (1997). Excess temperature of mantle plumes: The role of chemical  
725 stratification across D. *Geophysical Research Letters*, 24(13), 1583–1586. doi:  
726 10.1029/97GL01548
- 727 Farnetani, C. G., & Samuel, H. (2005). Beyond the thermal plume paradigm. *Geo-  
728 physical Research Letters*, 32(7), 1–4. doi: 10.1029/2005GL022360
- 729 French, S. W., & Romanowicz, B. (2015). Broad plumes rooted at the base of the  
730 Earth’s mantle beneath major hotspots. *Nature*, 525(7567), 95–99. doi: 10  
731 .1038/nature14876
- 732 Garnero, E. J., & McNamara, A. K. (2008). Structure and Dynamics of Earth’s  
733 Lower Mantle. *Science*, 320(5876), 626–628. doi: 10.1126/science.1148028
- 734 Girard, J., Amulele, G., Farla, R., Mohiuddin, A., & Karato, S. I. (2016). Shear  
735 deformation of bridgmanite and magnesiowüstite aggregates at lower mantle  
736 conditions. *Science*, 351(6269), 144–147. doi: 10.1126/science.aad3113
- 737 Griffiths, R. W., & Campbell, I. H. (1990). Stirring and structure in mantle start-  
738 ing plumes. *Earth and Planetary Science Letters*, 99(1-2), 66–78. doi: 10.1016/  
739 0012-821X(90)90071-5
- 740 Gülcher, A. J., Ballmer, M. D., & Tackley, P. J. (2021). Coupled dynamics and evo-  
741 lution of primordial and recycled heterogeneity in Earth’s lower mantle. *Solid  
742 Earth*, 12(9), 2087–2107. doi: 10.5194/se-12-2087-2021
- 743 Gülcher, A. J., Gebhardt, D. J., Ballmer, M. D., & Tackley, P. J. (2020). Vari-  
744 able dynamic styles of primordial heterogeneity preservation in the Earth’s  
745 lower mantle. *Earth and Planetary Sciences Letters*, 536(116160). doi:  
746 10.1016/j.epsl.2020.116160
- 747 Handy, M. R. (1994). Flow laws for rocks containing two non-linear viscous phases :  
748 a phenomenological approach. *Journal of Structural Geology*, 16(3), 287–301.
- 749 Hernlund, J. W., & Tackley, P. J. (2008). Modeling mantle convection in the spher-  
750 ical annulus. *Physics of the Earth and Planetary Interiors*, 171(1-4), 48–54.  
751 doi: 10.1016/j.pepi.2008.07.037
- 752 Herzberg, C., Condie, K., & Korenaga, J. (2010). Thermal history of the Earth and  
753 its petrological expression. *Earth and Planetary Science Letters*, 292(1-2), 79–  
754 88. doi: 10.1016/j.epsl.2010.01.022
- 755 Hinkel, N. R., Timmes, F. X., Young, P. A., Pagano, M. D., & Turnbull, M. C.  
756 (2014). Stellar abundances in the solar neighborhood: The hypatia catalog.  
757 *Astronomical Journal*, 148(3). doi: 10.1088/0004-6256/148/3/54
- 758 Hirose, K., Morard, G., Sinmyo, R., Umemoto, K., Hernlund, J. W., Helffrich,  
759 G. R., & Labrosse, S. (2017). Crystallization of silicon dioxide and com-  
760 positional evolution of the Earth’s core. *Nature*, 543(7643), 99–102. doi:  
761 10.1038/nature21367

- 762 Hirose, K., Sinmyo, R., & Hernlund, J. W. (2017). Perovskite in Earth's deep interior. *Science*, *738*(November), 734–738. doi: 10.1126/science.aam8561
- 763
- 764 Howard, L. N. (1964). Thermal convection at high Rayleigh number. In H. Görtler (Ed.), *Applied mechanics. proceedings of 11th international congress* (pp. 1109–1115). Berlin: Springer. doi: 10.1017/s0004972700024965
- 765
- 766
- 767 Hwang, Y. K., Ritsema, J., van Keken, P. E., Goes, S., & Styles, E. (2011). Wavefront healing renders deep plumes seismically invisible. *Geophysical Journal International*, *187*(1), 273–277. doi: 10.1111/j.1365-246X.2011.05173.x
- 768
- 769
- 770 Ito, E., & Sato, H. (1991). Aseismicity in the lower mantle by superplasticity of the descending slab. *Nature*, *351*(6322), 140–141. doi: 10.1038/351140a0
- 771
- 772 Jeanloz, R., & Morris, S. (1986). Temperature distribution in the crust and mantle. *Annual Review of Earth and Planetary Sciences*, *14*, 377–415.
- 773
- 774 Kaercher, P., Miyagi, L., Kanitpanyacharoen, W., Zepeda-Alarcon, E., Wang, Y., Parkinson, D., ... Wenk, H. R. (2016). Two-phase deformation of lower mantle mineral analogs. *Earth and Planetary Science Letters*, *456*, 134–145. Retrieved from <http://dx.doi.org/10.1016/j.epsl.2016.09.030> doi: 10.1016/j.epsl.2016.09.030
- 775
- 776
- 777
- 778
- 779 Karato, S., Riedel, M. R., & Yuen, D. A. (2001). Rheological structure and deformation of subducted slabs in the mantle transition zone: Implications for mantle circulation and deep earthquakes. *Physics of the Earth and Planetary Interiors*, *127*(1-4), 83–108. doi: 10.1016/S0031-9201(01)00223-0
- 780
- 781
- 782
- 783 Koelemeijer, P., Deuss, A., & Ritsema, J. (2017a). Density structure of Earth's lowermost mantle from Stoneley mode splitting observations. *Nature Communications*, *8*(May), 1–10. Retrieved from <http://dx.doi.org/10.1038/ncomms15241> doi: 10.1038/ncomms15241
- 784
- 785
- 786
- 787 Koelemeijer, P., Deuss, A., & Ritsema, J. (2017b). Density structure of Earth's lowermost mantle from Stoneley mode splitting observations. *Nature Communications*, *8*(May), 1–10. Retrieved from <http://dx.doi.org/10.1038/ncomms15241> doi: 10.1038/ncomms15241
- 788
- 789
- 790
- 791 Labrosse, S. (2002). Hotspots, mantle plumes and core heat loss. *Earth and Planetary Science Letters*, *199*(1-2), 147–156. doi: 10.1016/S0012-821X(02)00537-X
- 792
- 793
- 794 Larson, R. L., & Olson, P. (1991). Mantle plumes control magnetic reversal frequency. *Earth and Planetary Science Letters*, *107*, 437–447.
- 795
- 796 Lay, T., Hernlund, J., & Buffett, B. A. (2008). Core – mantle boundary heat flow. *Nature Geoscience*, *1*, 25–32.
- 797
- 798 Li, M., & Zhong, S. (2017). The source location of mantle plumes from 3D spherical models of mantle convection. *Earth and Planetary Science Letters*, *478*, 47–57. Retrieved from <http://dx.doi.org/10.1016/j.epsl.2017.08.033> doi: 10.1016/j.epsl.2017.08.033
- 799
- 800
- 801
- 802 Li, Y., Deschamps, F., & Tackley, P. J. (2014). The stability and structure of primordial reservoirs in the lower mantle: Insights from models of thermochemical convection in three-dimensional spherical geometry. *Geophysical Journal International*, *199*(2), 914–930. doi: 10.1093/gji/ggu295
- 803
- 804
- 805
- 806 Lin, S. C., & Van Keken, P. E. (2006). Dynamics of thermochemical plumes: 2. Complexity of plume structures and its implications for mapping mantle plumes. *Geochemistry, Geophysics, Geosystems*, *7*(3). doi: 10.1029/2005GC001072
- 807
- 808
- 809
- 810 Massmeyer, A., Di Giuseppe, E., Davaille, A., Rolf, T., & Tackley, P. J. (2013). Numerical simulation of thermal plumes in a Herschel-Bulkley fluid. *Journal of Non-Newtonian Fluid Mechanics*, *195*, 32–45. doi: 10.1016/j.jnnfm.2012.12.004
- 811
- 812
- 813
- 814 McKenzie, D. (1979). Finite deformation during fluid flow. *Geophys. J. R. astr. Soc.*, *58*, 689–715.
- 815
- 816 McNamara, A. K. (2019). A review of large low shear velocity provinces and ultra

- low velocity zones. *Tectonophysics*, 760(August 2017), 199–220. doi: 10.1016/j.tecto.2018.04.015
- Miyagoshi, T., Kameyama, M., & Ogawa, M. (2017). Extremely long transition phase of thermal convection in the mantle of massive super-Earths—. *Earth, Planets and Space*, 69(46). doi: 10.1186/s40623-017-0630-6
- Morgan, W. J. (1971). Convection plumes in the lower mantle. *Nature*, 230(5288), 42–43. doi: 10.1038/230042a0
- Mundl, A., Touboul, M., Jackson, M. G., Day, J. M., Kurz, M. D., Lekic, V., . . . Walker, R. J. (2017). Tungsten-182 heterogeneity in modern ocean island basalts. *Science*, 356(6333), 66–69. doi: 10.1126/science.aal4179
- Nakagawa, T. (2020). A coupled core-mantle evolution: review and future prospects. *Progress in Earth and Planetary Science*, 7(1). doi: 10.1186/s40645-020-00374-8
- Nakagawa, T., & Buffett, B. A. (2005). Mass transport mechanism between the upper and lower mantle in numerical simulations of thermochemical mantle convection with multicomponent phase changes. *Earth and Planetary Science Letters*, 230(1-2), 11–27. doi: 10.1016/j.epsl.2004.11.005
- Nakagawa, T., Tackley, P. J., Deschamps, F., & Connolly, J. A. (2010). The influence of MORB and harzburgite composition on thermo-chemical mantle convection in a 3-D spherical shell with self-consistently calculated mineral physics. *Earth and Planetary Science Letters*, 296(3-4), 403–412. doi: 10.1016/j.epsl.2010.05.026
- Ogawa, M. (2003). Chemical stratification in a two-dimensional convecting mantle with magmatism and moving plates. *Journal of Geophysical Research*, 108(B12). doi: 10.1029/2002jb002205
- Olson, P. (1990). Hot spots, swells and mantle plumes. In M. P. Ryan (Ed.), *Magma transport and storage* (pp. 33–51). Wiley.
- Olson, P., Schubert, G., & Anderson, C. (1993). Structure of axisymmetric mantle plumes. *Journal of Geophysical Research*, 98(B4), 6829–6844.
- Richards, M. A., Duncan, R. A., & Courtillot, V. E. (1989). Flood basalts and hot-spot tracks: Plume heads and tails. *Science*, 246(4926), 103–107. doi: 10.1126/science.246.4926.103
- Ritsema, J., Maguire, R., Cobden, L., & Goes, S. (2021). Seismic Imaging of Deep Mantle Plumes. In H. Marquardt, M. D. Ballmer, S. Cottaar, & J. G. Konter (Eds.), *Mantle convection and surface expressions* (pp. 353–369). AGU Monograph Series 263. doi: 10.1002/9781119528609.ch14
- Schubert, G., Masters, G., Olson, P., & Tackley, P. (2004). Superplumes or plume clusters? *Physics of the Earth and Planetary Interiors*, 146(1-2), 147–162. doi: 10.1016/j.pepi.2003.09.025
- Sleep, N. H. (1990). Hotspots and mantle plumes: some phenomenology. *Journal of Geophysical Research*, 95(B5), 6715–6736. doi: 10.1029/JB095iB05p06715
- Solomatov, V. S., & Reese, C. C. (2008). Grain size variations in the Earth’s mantle and the evolution of primordial chemical heterogeneities. *Journal of Geophysical Research: Solid Earth*, 113(7), 1–21. doi: 10.1029/2007JB005319
- Spaargaren, R. J., Ballmer, M. D., Bower, D. J., Dorn, C., & Tackley, P. J. (2020). The influence of bulk composition on the long-term interior-atmosphere evolution of terrestrial exoplanets. *Astronomy and Astrophysics*, 643, 1–13. doi: 10.1051/0004-6361/202037632
- Stevenson, D. J. (2003). Planetary magnetic fields. *Earth and Planetary Science Letters*, 208(1-2), 1–11. doi: 10.1016/S0012-821X(02)01126-3
- Tackley, P. J. (2000a). Self-consistent generation of tectonic plates in three-dimensional mantle convection 1. pseudoplastic yielding. *Geochemistry, Geophysics, Geosystems*, 1(1), 9–22. doi: 10.1016/S0012-821X(98)00029-6
- Tackley, P. J. (2000b). Self-consistent generation of tectonic plates in time-dependent, three-dimensional mantle convection simulations 2. strain weak-

- 872 ening and asthenosphere. *Geochemistry, Geophysics, Geosystems*, 1. doi:  
873 10.1029/2000gc000036
- 874 Tackley, P. J. (2008). Modelling compressible mantle convection with large viscosity  
875 contrasts in a three-dimensional spherical shell using the yin-yang grid. *Physics*  
876 *of the Earth and Planetary Interiors*, 171(1-4), 7–18. doi: 10.1016/j.pepi.2008  
877 .08.005
- 878 Tackley, P. J. (2012). Dynamics and evolution of the deep mantle resulting from  
879 thermal, chemical, phase and melting effects. *Earth-Science Reviews*, 110(1-4),  
880 1–25. doi: 10.1016/j.earscirev.2011.10.001
- 881 Tackley, P. J., Ammann, M. W., Brodholt, J. P., Dobson, D. P., & Valencia,  
882 D. (2013). Mantle dynamics in super-Earths: Post-perovskite rheol-  
883 ogy and self-regulation of viscosity. *Icarus*, 225(1), 50–61. doi: 10.1016/  
884 j.icarus.2013.03.013
- 885 Thielmann, M., Golabek, G. J., & Marquardt, H. (2020). Ferropericlasite control  
886 of lower mantle rheology: Impact of phase morphology. *Geochemistry, Geo-*  
887 *physics, Geosystems*, 21(e2019GC008688). doi: 10.1029/2019gc008688
- 888 Torsvik, T. H., Burke, K., Steinberger, B., Webb, S. J., & Ashwal, L. D. (2010).  
889 Diamonds sampled by plumes from the core-mantle boundary. *Nature*,  
890 466(7304), 352–355. Retrieved from [http://dx.doi.org/10.1038/](http://dx.doi.org/10.1038/nature09216)  
891 [nature09216](http://dx.doi.org/10.1038/nature09216) doi: 10.1038/nature09216
- 892 Torsvik, T. H., Svensen, H. H., Steinberger, B., Royer, D. L., Jerram, D. A., Jones,  
893 M. T., & Domeier, M. (2021). Connecting the Deep Earth and the Atmo-  
894 sphere. In H. Marquardt, M. D. Ballmer, S. Cottaar, & J. G. Konter (Eds.),  
895 *Mantle convection and surface expression* (pp. 413–453). Geophysical Monog-  
896 raphy Series 263. doi: 10.1002/9781119528609.ch16
- 897 Torsvik, T. H., Van Der Voo, R., Doubrovine, P. V., Burke, K., Steinberger, B.,  
898 Ashwal, L. D., ... Bull, A. L. (2014). Deep mantle structure as a refer-  
899 ence frame for movements in and on the Earth. *Proceedings of the National*  
900 *Academy of Sciences of the United States of America*, 111(24), 8735–8740. doi:  
901 10.1073/pnas.1318135111
- 902 Tschauner, O., Huang, S., Yang, S., Humayun, M., & Liu, W. (2021). Discovery of  
903 davemaoite, CaSiO<sub>3</sub>-perovskite, as a mineral from the lower mantle. *Science*,  
904 894(November), 891–894.
- 905 van Hunen, J., Zhong, S., Shapiro, N. M., & Ritzwoller, M. H. (2005). New evidence  
906 for dislocation creep from 3-D geodynamic modeling of the Pacific upper man-  
907 tle structure. *Earth and Planetary Science Letters*, 238(1-2), 146–155. doi:  
908 10.1016/j.epsl.2005.07.006
- 909 van Keken, P. E. (1997). Evolution of starting mantle plumes: a comparison be-  
910 tween numerical and laboratory models. *Earth and Planetary Science Letters*,  
911 148(97).
- 912 Whitehead, J. A., & Luther, D. S. (1975). Dynamics of laboratory diapir and  
913 plume models. *Journal of Geophysical Research*, 80(5), 705–717. doi:  
914 10.1029/jb080i005p00705
- 915 Wicks, J. K., & Duffy, T. S. (2016). Crystal Structures of Minerals in the Lower  
916 Mantle. *Deep Earth: Physics and Chemistry of the Lower Mantle and Core*,  
917 69–87. doi: 10.1002/9781118992487.ch6
- 918 Wilson, J. T. (1963). *A possible origin of the Hawaiian Islands* (Vol. 51) (No. 3).  
919 doi: 10.1139/cjes-2014-0036
- 920 Wolfe, C. J., Solomon, S. C., Laske, G., Collins, J. A., Detrick, R. S., Orcutt,  
921 J. A., ... Hauri, E. H. (2009). Mantle shear-wave velocity structure  
922 beneath the Hawaiian hot spot. *Science*, 326(5958), 1388–1390. doi:  
923 10.1126/science.1180165
- 924 Xie, S., & Tackley, P. J. (2004). Evolution of U-Pb and Sm-Nd systems in numerical  
925 models of mantle convection and plate tectonics. *Journal of Geophysical Re-*  
926 *search: Solid Earth*, 109(11), 1–22. doi: 10.1029/2004JB003176

- 927 Xu, W., Lithgow-Bertelloni, C., Stixrude, L., & Ritsema, J. (2008). The effect of  
 928 bulk composition and temperature on mantle seismic structure. *Earth and*  
 929 *Planetary Science Letters*, *275*(1-2), 70–79. doi: 10.1016/j.epsl.2008.08.012
- 930 Yamazaki, D., Inoue, T., Okamoto, M., & Irifune, T. (2005). Grain growth kinetics  
 931 of ringwoodite and its implication for rheology of the subducting slab. *Earth*  
 932 *and Planetary Science Letters*, *236*(3-4), 871–881. doi: 10.1016/j.epsl.2005.06  
 933 .005
- 934 Yamazaki, D., & Karato, S. I. (2001). Some mineral physics constraints on the rhe-  
 935 ology and geothermal structure of Earth’s lower mantle. *American Mineralo-*  
 936 *gist*, *86*(4), 385–391. doi: 10.2138/am-2001-0401
- 937 Yan, J., Ballmer, M. D., & Tackley, P. J. (2020). The evolution and distribu-  
 938 tion of recycled oceanic crust in the Earth’s mantle: Insight from geody-  
 939 namic models. *Earth and Planetary Science Letters*, *537*(March). doi:  
 940 10.1016/j.epsl.2020.116171